

Article

Combined Steam and CO₂ Reforming of Methane over Ni-Based CeO₂-MgO Catalysts: Impacts of Preparation Mode and Pd Addition

 Lyudmila Okhlopkova ^{1,*}, Igor Prosvirin ^{1,*}, Mikhail Kerzhentsev ¹ and Zinfer Ismagilov ^{1,2}
¹ Boreskov Institute of Catalysis SB RAS, Prospekt Akademika Lavrentieva 5, Novosibirsk 630090, Russia; mila65@catalysis.ru (L.O.); ma_k@catalysis.ru (M.K.); iccms@iccms.sbras.ru (Z.I.)

² Institute of Coal Chemistry and Material Science, Prospekt Soviet 18, Kemerovo 650000, Russia

* Correspondence: prosvirin@catalysis.ru; Tel.: +7-383-326-9774

Abstract: The sol–gel template technique makes it possible to synthesize a stable and efficient nickel catalyst based on magnesium-modified cerium oxide Ce_{0.5}Mg_{0.5}O_{1.5} for the combined steam and CO₂ reforming of methane. To stabilize dispersed forms of the active component in the matrix of the support, the catalysts were synthesized by changing the support precursor (cerium acetate and chloride), the active component composition (Ni, NiPd) and the method of introducing nanoparticles. The relationship was established between the physicochemical and catalytic characteristics of the samples. The use of cerium acetate as a support precursor provided smaller pore and crystallite sizes of the support, a stabilization of the dispersed forms of the active component, and excellent catalytic characteristics. The introduction of Pd into the Ni nanoparticles (Pd/Ni = 0.03) increased the resistance of the active component to sintering during the reaction, ensuring stable operation for 25 h of operation. The increased stability was due to a higher concentration of defective oxygen, a higher dispersion of bimetallic NiPd nanoparticles, and the Ni clusters strongly interacting with the NiO-MgO solid solution. An efficient and stable Ni_{0.194}Pd_{0.006}Ce_{0.4}Mg_{0.4}O_{1.4} catalyst for the conversion of CO₂ into important chemicals was developed. With the optimal composition and synthesis conditions of the catalyst, the yield of the target products was more than 75%.

Keywords: H₂O/CO₂ methane reforming; Ni-CeO₂-MgO; sol–gel; Pd promotion; dispersion



Citation: Okhlopkova, L.; Prosvirin, I.; Kerzhentsev, M.; Ismagilov, Z. Combined Steam and CO₂ Reforming of Methane over Ni-Based CeO₂-MgO Catalysts: Impacts of Preparation Mode and Pd Addition. *Appl. Sci.* **2023**, *13*, 4689. <https://doi.org/10.3390/app13084689>

Academic Editors: Elena Korznikova and Andrey Kistanov

Received: 16 March 2023

Revised: 5 April 2023

Accepted: 6 April 2023

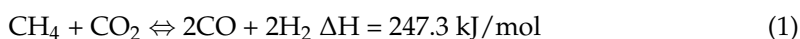
Published: 7 April 2023



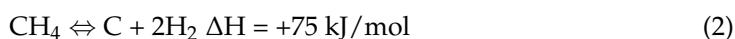
Copyright: © 2023 by the authors. Licensee MDPI, Basel, Switzerland. This article is an open access article distributed under the terms and conditions of the Creative Commons Attribution (CC BY) license (<https://creativecommons.org/licenses/by/4.0/>).

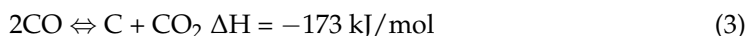
1. Introduction

The preferred use of fossil fuels to meet energy demands has created environmental concerns due to significant emissions of environmentally harmful gases (CO₂ and CH₄). In addition, the depletion of fossil fuel reserves puts humanity in front of the need for tough energy conservation and the use of new resource-saving technologies [1,2]. Converting CO₂ into value-added chemicals or fuels is the background of the sustainable development of the chemical industry and contributes to the reduction of CO₂ emissions. CH₄ is contained in significant quantities in associated gas and in renewables. CH₄ can react with a reducing agent, CO₂, a technique known as dry methane reforming (DMR, Equation (1)) [3].

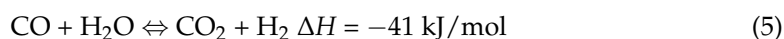
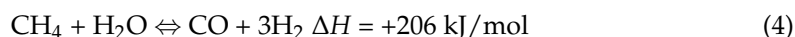


DMR simultaneously converts two greenhouse gases and the resulting gas mixture of H₂ and CO (synthesis gas can be used as a fuel or feedstock in the Fischer–Tropsch process [4]), for the production of valuable products such as methanol, dimethyl ether, and acetic acid [5,6] and for the storage of nuclear and solar energy [3]. The well-proven technology for the fabrication of syngas by the DRM reaction in the presence of catalysts has its drawbacks, associated with the easy poisoning of the catalyst by coke (Equations (2) and (3)):





Adding steam to the DMR process is an effective way to limit soot formation and increase the ratio H_2/CO [7,8]. H_2O is an inexpensive and abundant resource that reacts with CH_4 via steam-methane reforming (SMR—Equation (4)) and combines with the steam-CO reforming reaction (Equation (5)) to produce H_2 :



Combining DMR with SMR provides two key advantages over single DMR reactions, namely: (i) H_2O increases the O/C ratio in the feed, which promotes soot oxidation; (ii) H_2O provides additional H atoms to form H_2 , thereby adjusting the H_2/CO molar ratio in the product stream.

Due to the chemical stability of both CO_2 and CH_4 , the reaction of DMR and $\text{H}_2\text{O}/\text{CO}_2$ reforming of methane (CSMR) is usually performed at 800–1000 °C in the presence of a catalyst containing platinum group metals (for example, Rh [9], Ru [10,11], Pd [12,13] and Pt [14,15]) or a base-metal catalyst (Fe, Co or Ni) [16–19]. Low-cost and active Ni-based catalysts have the most potential for wide industrial use. The Ni dispersion, oxygen vacancy (V_o) concentration and the interaction between Ni and its support affect the CSMR performance. An increase in dispersion and, as a result, an expansion of the number of active points promote catalytic performance [20]. Reducible oxides, such as CeO_2 , have been used as supports or promoters to obtain catalysts with a high content of oxygen defects [21,22]. It is believed that V_o on metal oxides are active centers of CO_2 activation [23,24]. These vacancies reduce the activation energy of CO_2 by providing electrons. The high oxygen (O_x) and vacant mobility of ceria and the Ni–ceria interface are responsible for burning carbon via the following reactions: $\text{C} + \text{O}_x = \text{CO} + V_o + 2e$ [25]. The disadvantages of Ni catalysts include the decrease in activity when used for a long time as a result of the formation of carbon deposits and the sintering of the active component at high reaction temperatures. A huge role of the support is realized through the strong interaction with metal providing a high resistance to coking and preventing metal sintering [26]. The main properties of the MgO-containing support contribute to an increase in steam adsorption [27], the prevention of coke formation resulting from its basicity [28–31], and the strong interaction with the solid solution $\text{Ni}_y\text{Mg}_{1-y}\text{O}$ ($y = 0.02 - 0.15$) [32]. Since 1990, for the DMR process, it has been proposed to use the sol–gel templated method (SGT) to prepare the support with an ordered pore structure, a high thermal stability and a specific surface area, giving the opportunity to control the formation of nanoparticles of a certain size and increase their availability [33–35].

It has been shown that the doping of nickel catalysts with a small quantity of noble metals (Pt, Pd, Rh, Ru) is a promising approach to the development of catalysts with excellent characteristics for methane reforming [36]. The improvement of the catalytic properties of the catalytic performance is explained in terms of activity, inhibition of nickel oxidation, self-activation, carbon formation [8,15,36–39]. The catalytic properties of Pt–Ni/ CeO_2 were improved due to the synergistic effect between the two metals affecting the dispersion of the metals, the reduction properties, and the stabilization of the surface structure of the active assemblies [15]. To increase the stability of catalysts, it was proposed not only to increase the mobile oxygen concentration, but also to add a noble metal, which promotes the activation of CO_2 and the gasification of coke. With the addition of noble metals, a performance improvement can be achieved due to a *synergies* of metal and support (metal promotes the reducibility of CeO_2 , while CeO_2 stabilizes the Ni dispersion [40]) and a decrease in the rate of formation and change in the type of carbon deposits [15,37]. A DFT calculation has showed that the CO gas evolution reaction, which suppresses carbon deposition and improves the catalytic efficiency of H_2 formation, is facilitated on the Ni–Ru alloy [41]. The synergistically increased catalytic activity must be explained

by unexpected geometric and electronic effects between the two kinds of metals [42–46]. By carefully choosing the preparation method, one can obtain bimetallic particles with different structures (segregated and well-mixed structured) [36].

Thus, a mesoporous support based on CeO₂-MgO combines the ability to stabilize highly dispersed structures of the active component and generate/transfer reactive species for the oxidation of carbon-containing intermediates formed on Ni catalytic sites. In this article, in order to develop a deactivation-resistant nickel-based CSMR process catalyst, a comparative study of the formation X/Ce_{0.5}Mg_{0.5}O_{1.5} (X = 10% wt.% Ni, 10% wt.% Ni-0.5% wt.% Pd) prepared by the SGT method, depending on a support precursor and the support functionalization method (one-stage synthesis and polyol method), was performed. The catalyst with 10 wt.% Ni was chosen as optimal by analogy with the 10%Ni/CeO₂ catalyst, which possessed a stability to coke deposition and sintering [47]. To prepare bimetallic particles with well-mixed structures, the polyol method was used [48]. Based on the results from this work, it is possible to suggest an approach for improving the performance of Ni-based catalysts in CSMR for syngas production.

2. Materials and Methods

2.1. Chemicals and Material

Polyvinylpyrrolidone (PVP), with an average molecular weight of 58,000 was purchased from Acros Organics (Geel, Belgium). Ni(CH₃COO)₂·4H₂O (98%) was purchased from Reachim (Moscow, Russia). Anhydrous ethylene glycol (99.5%) and 1,4-dioxane (99.9%) were purchased from Soyuzkhimprom (Novosibirsk, Russia). Pd(CH₃COO)₂ (46.5% Pd) was purchased from Aurat (Moscow, Russia). NaOH (99%), Ni(NO₃)₂·6H₂O (99%), Mg(NO₃)₂·6H₂O (98%) and CeCl₂·7H₂O (98%) were purchased from Vekton (Saint Petersburg, Russia). Ethanol (99.9%, HPCL grade) was purchased from J.T.Baker (Deventer, The Netherlands). Pluronic F127 (PEO₁₀₆PPO₇₀PEO₁₀₆, MW = 12,600) was purchased from Sigma-Aldrich (St. Louis, MO, USA). Ce (CH₃COO)₂·1.5H₂O (99.9%) was purchased from Alfa Aesar, Karlsruhe, Germany). All compounds were utilized without being purified further.

2.2. Methods for Preparing Catalysts

X_{0.2}Ce_{0.4}Mg_{0.4}O_{1.4} catalyst samples (X = Ni, Ni_{0.97}P_{0.03}) were prepared by the SGT method assisted with Pluronic F127 by varying the support precursor (cerium acetate and chloride); the method of introducing nanoparticles was as follows: a S-series, in which nanoparticles were incorporated at the stage of sol formation (one-stage synthesis), and a P-series, in which nanoparticles were obtained by the polyol technique (PT) in the presence of a support. The nickel and palladium concentrations were 10 wt.% and 0.5%, respectively.

Colloidal solutions of Ni-Pd nanoparticles (molar ratio Pd/Ni = 0.03) were synthesized by PT. Polyvinylpyrrolidone (PVP) was dissolved in anhydrous ethylene glycol, a calculated amount of Ni(CH₃COO)₂·4H₂O was added, and the mixture was heated to 80 °C for 2 h. The calculated amount of Pd(CH₃COO)₂ was dissolved in 1,4-dioxane with vigorous stirring for 2 h. Then, the first solution was cooled to 0 °C in an ice bath and the solution of Pd precursor was added thereto while stirring. A 1 M NaOH solution was added to adjust the pH of the mixture to 9–10. The resulting solution was heated for 2 h.

In the S-series, the colloid precipitate Ni-Pd or Ni(NO₃)₂·6H₂O was dissolved by stirring in ethanol. Then, Pluronic F127 dissolved in ethanol was added. A solution of CeCl₂·7H₂O or Ce (CH₃COO)₂·1.5H₂O and Mg(NO₃)₂·6H₂O in ethanol and water was added under stirring. The molar ratio of the reagents in CeO₂ was 0.5CeCl₂·7H₂O (Ce(CH₃COO)₂·1.5H₂O):0.5Mg(NO₃)₂:0.009F127:10H₂O:25C₂H₅OH. The sol prepared from cerium acetate was placed in an oven at 40 °C and 50% humidity for 2 days until gel formation, then dried for 1 day at 60 °C and 1 day at 100 °C. To remove the surfactant, the samples were calcined in two ways: without access to air and in air. In the first case, the sol was dried in a vacuum oven at 300 °C and a pressure of 13 mbar for 2 h at a heating rate (HR) of 1 °C/min. The sol (prepared from both chloride and cerium acetate) was transferred

to an oven, the furnace temperature was increased to 200 °C at an HR of 20 °C/min; then, the temperature was increased to 500 °C at an HR of 1 °C/min; at that temperature the samples were heated for 2 h to stabilize the mesoporous structure.

In the P-synthesis, the prepared support was added to a solution of PVP and Ni(CH₃COO)₂·4H₂O in ethylene glycol. The supports were prepared by the SGT method. Then, the suspension was cooled to 0 °C in an ice bath and the pH of the mixture was adjusted to 9–10 with a 1 M NaOH solution. The resulting solution was heated for 2 h with vigorous mixing. The composition of the mixture was 0.5Ce(CH₃COO)₂·1.5H₂O:0.5Mg(NO₃)₂:0.009 F127:10H₂O:25C₂H₅OH. The sol was transferred to a vacuum oven, heated to 200 °C for 2 h; the HR was 1 °C/min. Then, the catalyst was placed in an oven, heated to 200 °C with an HR of 20 °C/min. The temperature was increased to 500 °C; the HR was 1 °C/min; at that temperature, the sample was heated for 4 h to stabilize the mesoporous structure.

The samples were marked in accordance with the procedure for their synthesis: the first letter denoted the support precursor, where “A” and “C” corresponded to acetate and cerium chloride, and “S” and “P” corresponded to samples obtained by one-stage and polyol methods, respectively. The third letter denoted the activation conditions: “O” and “V” for the activation in air and in vacuum, respectively. For example, Ni-Pd/CeMg-A-S-V was a sample prepared from cerium acetate by a one-stage method based on Ni_{0.97}Pd_{0.03} nanoparticles and calcined in vacuum at 500 °C for 2 h, then in air at 500 °C for 4 h. In some cases, the heat treatment of the catalysts was carried out at two temperatures (700 °C or 900 °C) in air for 4 h. Characterization techniques, such as BET surface measurement, X-ray diffraction (XRD), X-ray photoelectron spectroscopy (XPS), and thermogravimetric analysis (TGA) were used to elucidate the effect of preparation conditions on the catalytic properties and establish a correlation with catalytic performance in the CSMR, their description is given in Supplementary Materials.

2.3. Methods for Studying the Activity of Catalysts

The CSMR reaction took place in a fixed-bed reactor having an inner/outer diameter and lengths of 30/35 mm and 70 cm, respectively (Figure S1). The activity of catalysts in the CSMR under the following reaction conditions [49]: catalyst loading—0.5 g, fraction—0.25 ÷ 0.5 mm, contact time—0.15 s, mixture feed rate—200 mL/min, temperature—600–800 °C, CH₄:CO₂:H₂O:He = 1.0:0.81:0.38:2.8. Under these conditions, the kinetic area of the reaction was achieved and no significant influence of external or internal diffusion was observed. The activity of the catalysts in the CSMR was characterized by the conversion of methane and carbon dioxide, the yields of hydrogen, carbon dioxide, and the H/CO molar ratio. Conversions and yields were calculated using the formulas:

$$X_{CH_4} = \frac{mol_{CH_4}^{in} - mol_{CH_4}^{out}}{mol_{CH_4}^{in}} \times 100$$

$$X_{CO_2} = \frac{mol_{CO_2}^{in} - mol_{CO_2}^{out}}{mol_{CO_2}^{in}} \times 100$$

$$Y_{CO} (\%) = \frac{mol_{CO}^{out}}{(mol_{CH_4}^{in}) + (mol_{CO_2}^{in})} \times 100$$

$$Y_{H_2} (\%) = \frac{mol_{H_2}^{out}}{2 \times (mol_{CH_4}^{in}) + (mol_{H_2O}^{in})} \times 100$$

Before the start of the reaction, the catalysts were activated in a flow of 30 vol.% H₂/He at 800 °C for 1 h. To determine the stability of the catalysts, their activity was studied for ~25 h in the CSMR. The screening tests were carried out in a mode with a stepwise

temperature increase in the range 650–850 °C. The HR was 10 °C/min; the exposure time at each temperature was 40 min. Stability tests were carried out for 24 h at 750 °C.

3. Results and Discussion

3.1. Physicochemical Research of Fresh Catalysts

The samples were prepared using various methods of functionalization of the oxide matrix: a one-stage synthesis where the active component was incorporated at the stage of sol formation (S-series), and the PT, where the formation of nanoparticles occurred in the presence of a support (P-series) using acetate and cerium chloride as a support precursor (Table 1). All synthesized materials had a type H3 hysteresis loop on their adsorption isotherm with a type IV (Figure S2) characteristic of adsorbents formed by plane-parallel particles. Indeed, it was shown by SEM that catalyst samples prepared from cerium chloride by a one-stage synthesis were irregularly shaped plates with a polydisperse pore system (Figure S3). The evaluation of the uniformity of the doping cation distribution using SEM confirmed the homogeneity of the materials obtained. The hysteresis at $p/p_0 = 0.5 \div 0.9$ indicated the presence of a predominantly textural mesoporosity [50]. Compared to the corresponding support, the catalysts showed a drop of BET surface areas (S_{BET}), pore volumes (V_{pore}), and average pore diameters (D_{pore}), which indicated that the NiO particles were located in the pores of the mesoporous CeO₂-MgO. In the differential pore distribution curve of the catalyst, the maximum shifted towards larger pore sizes and the curve broadened when cerium chloride was used instead of cerium acetate (SI, Figure S3). The Ni/CeMg-A-S-V samples prepared from cerium acetate by the one-stage synthesis and activated in vacuum had the narrowest distribution of pore sizes, being apparently associated with less pore clogging. D_{pore} increased when Ce(III) chloride was used as a support precursor, for an A catalyst calcined in air, and with a rise in the calcination temperature (Figure 1). In the first case, large pores were formed already at the stage of sol formation; in the second and third cases, the destruction of the mesoporous structure of the support proceeded with an increase in the activation temperature. The decomposition of support precursors was an exothermic reaction; the release of heat led to the combustion of the template in air and a spontaneous increase in temperature. D_{pore} of the Ni/CeMg-A-S-V and Ni/CeMg-A-S-O catalysts prepared from cerium acetate by the one-stage synthesis did not increase with increasing temperature (Figure 1). Thus, to create a stable mesoporous structure with a smaller pore size of Ni/CeMg catalysts, we had to use the one-stage synthesis, cerium acetate as a precursor, and an activation in vacuum.

Table 1. Textural properties of the support and as-prepared catalysts.

Sample	Textural Properties		
	$S_{\text{BET}}, \text{m}^2/\text{g}$	$V_{\text{pore}}, \text{cm}^3/\text{g}$	$D_{\text{pore}}, \text{nm}$
CeMg-A-S-V	77.9	0.12	5.1
Ni/CeMg-C-S-O	23.0	0.12	18.4
Ni/CeMg-A-S-V	13.9	0.05	9.4
Ni/CeMg-A-S-O	48.2	0.278	17.4
Ni-Pd/CeMg-A-S-V	21.1	0.06	8.3
Ni/CeMg _{0.5} -A-P-O	34.3	0.104	7.6

The influence of the oxide functionalization method and material composition on the forms of stabilization of the active component and its resistance to sintering by a complex of physicochemical methods was investigated. The analysis of the diffraction patterns showed that the phase composition of the samples was determined by the support precursor and the method of oxide matrix functionalization (Table 2). Patterns in Figure 2 demonstrate that samples contained the fluorite-structured CeO₂ (ICSD 621718). The unit cell parameter of CeO₂ ($a = 0.542 \text{ nm}$) decreased when cerium was replaced by magnesium cations with a smaller radius (0.74 \AA). The dependence of the lattice parameters on the ionic radius of the introduced cation may indicate the formation of a homogeneous solid solution. The

increased value of the CeO₂ lattice in the A catalyst (Table 1) was due to the higher content and diameter of Ce³⁺ (1.03 Å instead of 0.92 Å for Ce⁴⁺). The lattice expansion of CeO₂ increased the concentration of defects [51]. The peaks observed at 42.9 and 62.8° belonged to NiO (ICSD 24018) and/or MgO (ICSD 64929), which have similar diffraction patterns in that region. The particle sizes of NiO and CeO₂ decreased when cerium acetate was used as a support precursor (Figure 2). The estimation of the average size of crystalline domains from the NiO (111) phase at 37.2° and CeO₂ (200) phase at 33.2° according to the Debye–Scherrer equation showed that the size of the coherent scattering region (CSR) of CeO₂ varied from 6 to 19 nm, and for NiO, from 0 to 18 nm. Note that after calcination in vacuum at 300 °C and in air at 500 °C the samples had smaller pore and CeO₂/NiO crystallite sizes (Tables 1 and 2) compared to the samples calcined at 500 °C in air. Like Ni catalysts, bimetallic Ni-Pd sample had a highly dispersed state of the active component (Table 1).

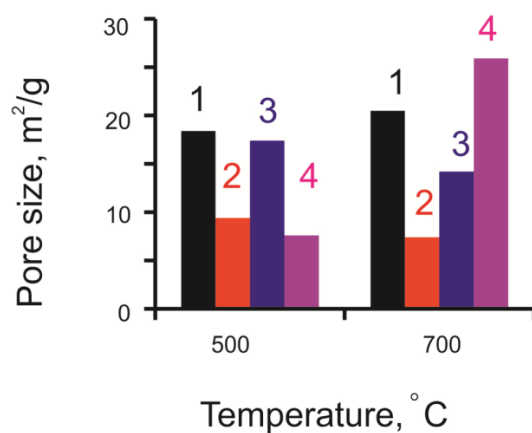


Figure 1. Influence of the calcination temperature on the D_{pore} prepared from cerium acetate. 1- Ni/CeMg-C-S-O, 2- Ni/CeMgO-A-S-V, 3- Ni/CeMg-A-S-O, 4- Ni/CeMg-A-P-O.

Table 2. Influence of the calcination temperature on the phase composition and dispersion of catalysts.

Sample	500 °C				700 °C			
	a_{CeO_2} , Å	d_{CeO_2} , nm	a_{NiO} , Å	d_{NiO} , nm	a_{CeO_2} , Å	d_{CeO_2} , nm	a_{NiO} , Å	d_{NiO} , nm
Ni/CeMg-C-S-O	5.393	21	4.20	17	5.394	29	4.196	40
Ni/CeMg-A-S-V	5.403	6	ND ¹	ND ¹	5.401	15	4.212	9
Ni/CeMg-A-S-O	5.400	17	4.17	14	5.406	21	4.185	19
Ni-Pd/CeMg-A-S-V	5.401	10	ND ¹	ND ¹	5.400	35	4.194	30
Ni/CeMg-A-P-O	5.397	19	4.17	18	5.404	36	4.185	40

¹ Not determined due to low intensity of the peak.

To study the thermal stability, the samples were calcined at 500 °C for 2 h in air, and the XRD patterns of the samples are shown in Figure S4. The structural parameters of the samples changed with the increase of the calcination temperature, the nature of which was determined by the preparation method (Table 2). The most dispersed sample was obtained from cerium acetate by the one-stage synthesis, which was consistent with the higher thermal stability of that sample. The particle sintering could be associated with a partial destruction of the mesoporous support structure. Obviously, the sintering of nanoparticles decreased with an increase of the support thermal stability. It was noted in [52] that heat-resistant materials with a small surface area were more suitable for the CSMR reaction; when using these supports, the agglomeration of active species and the occurrence of side reactions were reduced. The part of Mg that was not included in the CeO₂ structure [53] could interact with nickel to form a solid solution with a > 0.417 nm (0.4177 nm for NiO and 0.4213 nm for MgO) (Table 2). The interaction of NiO with MgO was less for Ni/CeMg-A-P-O, as confirmed by the lower a_{NiO} value.

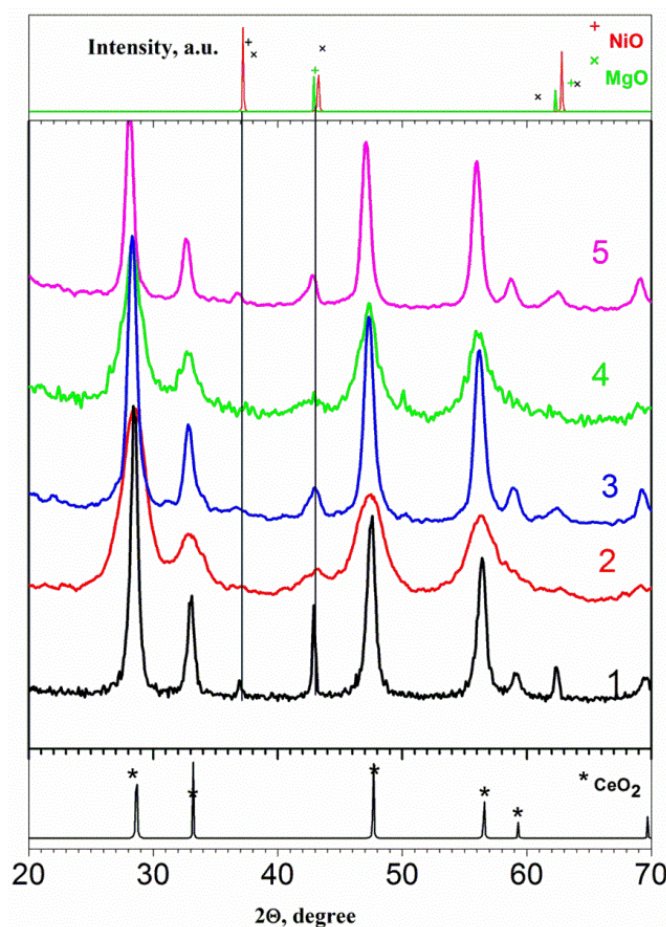


Figure 2. X-ray diffraction patterns of the as-prepared catalysts calcined at 500 °C. 1—Ni/CeMg-C-S-O; 2—Ni/CeMg-A-S-O; 3—Ni/CeMg-A-S-V; 4—Ni-Pd/CeMg-A-S-V; 5—Ni/CeMg-A-P-O.

3.2. The Characterization of the Reduced Catalysts

Since active sites for the CSMR reaction are Ni⁰ crystallites, the dispersion of the catalysts and their stability to sintering during activation of the NiO in a reducing atmosphere were examined by XRD (Figure 3, Table 3). The XRD patterns of all catalysts reduced at 800 °C for 2 h in an atmosphere of 30 vol.% H₂/He are shown in Figure 3. The as-reduced catalysts showed similar diffractograms compared to the pristine catalysts, while the corresponding peak intensities for cerium oxide were narrower, indicating an increase in crystallinity and nanoparticle size after reduction. The peak positions at 31.1° and 44.5° revealed the NaCl phase (ICSD 44277) in the reduced C catalyst. The phase composition of the catalysts after activation in an atmosphere of 30 vol.% H₂/He depended on the method of sample synthesis (Table 3). Ni²⁺ species in the C catalyst could not be reduced at the pretreatment of 800 °C under the 30 vol.% H₂/Ar atmosphere. Gao et al. found that chlorine ions prevented the reduction of Ni²⁺ ions and suppressed the adsorption of CO₂ [54]. The activation of the A-series catalysts led to the reduction of the NiO phase and the formation of the Ni⁰ phase (ICSD 646090) (Table 3, Figure 3). When comparing data for the Ni/CeMg samples reduced at 800 °C, the samples of the A-P-O and A-S-O series were characterized by a lower dispersion of Ni⁰, calculated from the Ni(111) phase at 44.3° using the Debye–Scherrer equation. Apparently, the Ni⁰-Ce_{0.5}Mg_{0.5}O_{1.5} interaction (MSI) was much weaker for the A-P-O and A-S-O samples, which ensured the agglomeration and reduction of Ni²⁺ in the process of their activation. The XRD study at an increase in temperature up to 800 °C showed that the resistance to sintering was higher in the case of the A-S-V samples.

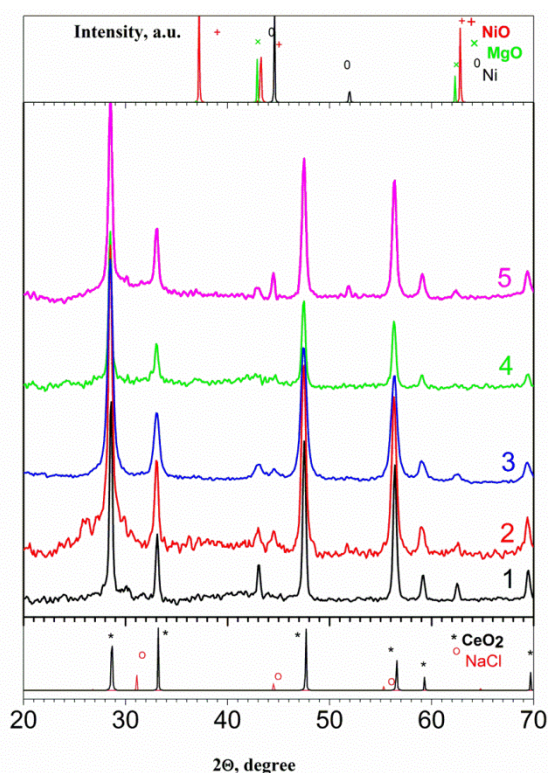


Figure 3. X-ray diffraction patterns of the catalysts reduced at 800 °C. 1—Ni/CeMg-C-S-O; 2—Ni/CeMg-A-S-V; 3—Ni/CeMg-A-S-O; 4—Ni-Pd/CeMg-A-S-V; 5—Ni/CeMg-A-P-O.

Table 3. Influence of the reduction temperature on the phase composition and dispersion of catalysts.

Sample	600 °C				800 °C			
	a_{CeO_2} , Å	d_{CeO_2} , nm	a_{NiO} , Å	d_{NiO} , nm	a_{CeO_2} , Å	d_{CeO_2} , nm	a_{NiO} , Å	d_{NiO} , nm
Ni/CeMg-C-S-O	5.399	44	4.20	49	-	5.410	50	4.20
Ni/CeMg-A-S-V	5.400	12	ND ¹	ND ¹	ND ¹	5.408	23	4.20
Ni/CeMg-A-S-O	5.401	12	ND ¹	ND ¹	12	5.406	32	4.18
Ni-Pd/CeMg-A-S-V	5.401	31	ND ¹	ND ¹	17	5.404	36	ND
Ni/CeMg-A-P-O	5.400	25	ND ¹	ND ¹	25	5.404	34	4.21

¹ Not determined due to low intensity of the peak.

To understand the effect of the support precursor, the activation mode, and the active component composition on the catalytic properties, an analysis of XPS spectra was carried out. Survey XPS spectra revealed the presence of Ni, Ce, Zr, and O for all prepared catalysts (Figure S5). In addition, the C catalyst contained Cl, which appeared as a peak at 199.4 eV. This was consistent with diffraction patterns of catalysts reduced and calcined at 800 °C showing the peak of NaCl at 31.6° and 45.3°. According to the XPS study, Ni existed in the form of Ni²⁺, which was confirmed by peaks at binding energies BE(Ni2p_{1/2}) = 873.9 eV and BE(Ni2p_{3/2}) = 856.7 eV and a shake-up satellite at about 861–862 eV (Figure S6). For the A catalysts, the peaks centered at 852.6 eV were assigned to Ni⁰. Ni was present as Ni²⁺ in the reduced C catalysts. This was in good agreement with the XRD data (Table 4). In addition, the surface concentration of nickel in this catalyst was much lower than in catalysts A. For Ni/CeMg-A-P-O, the ratio Ni/Ce was greater (Table 4) and the peak position of Ni²⁺ shifted to a lower BE compared to that of Ni-Pd/CeMg-A-S-V, Ni/CeMg-A-S-V, and Ni/CeMg-A-S-O (Figure S6), indicating that the polyol method ensured the weakening of the interaction between the Ni²⁺ and the Ce_{0.5}Mg_{0.5}O_{1.5} support and the location of nickel species on the surface. Spectra of Ce3d core (Figure 4) contained two sets of spin-orbit multiplets corresponding to a 3d_{5/2} and 3d_{3/2} ionization, respectively. The peaks at 880.5, 885.3, 904.2, and 899.9 belonged to Ce³⁺ (3d104f1 state of Ce₂O₃), while the other peaks

at 882.3, 888.8, 898.2, 901.0, 907.2, and 916.7 could be attributed to Ce^{4+} ($3d104f0$ state of CeO_2) [55]. This showed the presence of both Ce^{3+} and Ce^{4+} . The relative concentrations of $\text{Ce}^{3+}/\text{Ce}^{4+}$ are summarized in Table 4. The A catalysts had a higher Ce^{3+} concentration compared to the C-series catalysts. In that case, each XPS peak O1s could be decomposed into three components (Figure 5) [31]. Peaks at 529.4, 531.5, and 533.1 eV corresponded to lattice oxygen, defective oxygen on the CeO_2 surface, and adsorbed OH or H_2O particles, respectively (Table 4). The Ni-Pd/CeMg-A-S-V and Ni/CeMg-A-S-V catalysts had a higher content of defective oxygen, and more concentration of V_o . V_o improves the adsorption of CO_2 through the formation of bicarbonates [24] and is necessary for the CO_2 reforming of CH_4 [56]. In addition, the C catalysts showed a lower concentration of defective oxygen (CDO) than the A catalysts, caused by the lower Ce^{3+} contents. The surface molar ratio of $\text{Ni}^0/\text{Ni}^{2+}$ increased in the series Ni-Pd/CeMg-A-S-V < Ni/CeMg-A-S-V < Ni/CeMg-A-S-O < Ni/CeMg-A-P-O. As shown in refs. [57,58], the intensity of reoxidation increases with an increase in the dispersion and degree of MSI.

Table 4. XPS results of catalysts.

Sample	$\text{Ce}^{3+}/\text{Ce}^{4+}$ ¹	Concentration of Defective Oxygen (%) ²	Ni/Ce	$\text{Ni}^0/\text{Ni}^{2+}$ ³
Ni/CeMg-C-S-V	0.19	17.3	0.06	0
Ni/CeMg-A-S-V	0.25	28.4	0.52	0.72
Ni/CeMg-A-S-O	0.23	26.6	0.32	0.67
Ni-Pd/CeMg-A-S-V	0.28	32.7	0.41	0.63
Ni/CeMg-A-P-O	0.22	28.1	1.3	0.77

¹ Calculated from XPS Ce 3d spectra. ² Calculated from XPS O 1s spectra. ³ Calculated from XPS Ni 2p spectra.

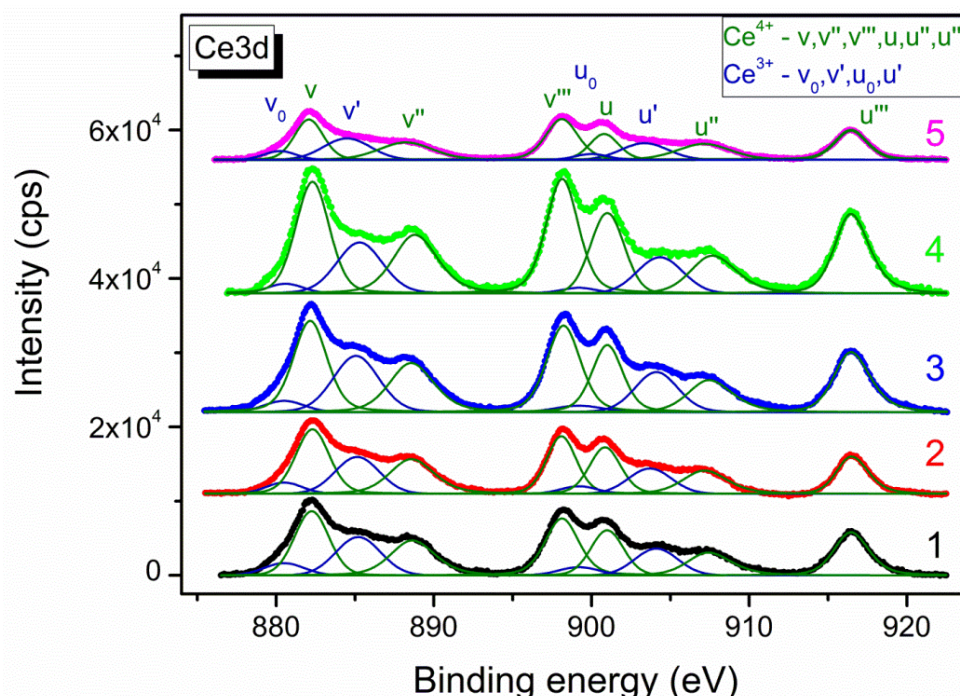


Figure 4. Ce3d XPS spectra of the catalysts reduced at 800 °C. 1—Ni/CeMg-C-S-O; 2—Ni/CeMg-A-S-O; 3—Ni/CeMg-A-S-V-500; 4—Ni-Pd/CeMg-A-S-V, 5—Ni/CeMg-A-P-O.

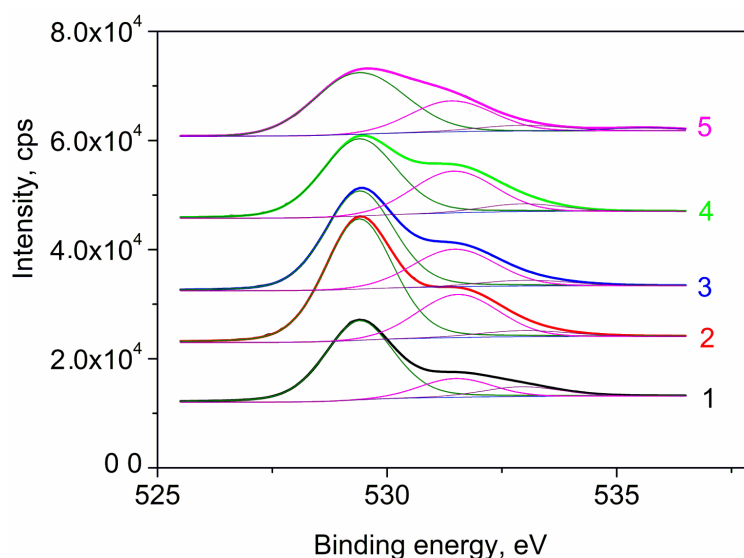


Figure 5. O1s X-ray photoelectron spectra of the catalysts reduced at 800 °C. 1—Ni/CeMg-C-S-O; 2—Ni/CeMg-A-S-O; 3—Ni/CeMg-A-S-V-500; 4—Ni-Pd/CeMg-A-S-V, 5—Ni/CeMg-A-P-O.

3.3. Catalytic Performance

Since CSMR is an endothermic reaction, the conversion of CH₄ increases with an increase in the reaction temperature. According to Figure S7, the CH₄ conversion was gradually growing with the increasing temperature (from 600 °C to 850 °C). This is consistent with the literature data [59–61] and indicates that the concentration of Ni⁰ active centers in the CSMR reaction increases with an increasing temperature. The conversion of CH₄, CO₂, and the yields of H₂ and CO increased with the increasing temperature of the reaction. The H₂/CO ratio was less than the calculated one (1.64 at a given value of CO₂ + H₂O/CH₄). We can explain this fact by the water gas conversion reaction; as a result, H₂ was consumed, and CO was formed (Figure S8). Moreover, the decrease in the H₂/CO ratio at higher temperatures may be owing to a preferable course of DRM. As shown in Table 5, the indicators of the CSMR reaction at 750 °C depended on the method of preparing the catalysts. For the Ni/CeMg samples, the hydrogen yield increased in the series of the support precursor C < A, and for samples from series A, in the series A-P-O < A-S-O ~ A-S-V, which was not similar to the dispersion row of the reduced catalysts A-S-P < A-S-O < A-S-V (Table 3). The initial activity of the A-S-O and A-S-V catalysts was very close. Therefore, we can conclude that the size effect (d) estimated by XRD on the initial catalytic activity was weak. It was shown in [62,63] that coordinative unsaturated surface atoms, which predominate in small crystallites (d < 10 nm), are much more active in methane reforming reactions than atoms in planes with low crystallographic indices in large crystallites. When d is greater than 12 nm, the fraction of active Ni⁰ species will not significantly change.

Table 5. Initial activity in CSMR at 750 °C, XRD and thermal analysis data after 24 h on stream in CSMR at 750 °C.

Sample	Indicators of the Reaction at 750 °C					XRD Data				TA Data after Reaction	
	X _{CH4}	X _{CO2}	Y _{H2}	Y _{CO}	H ₂ /CO	a _{CeO2} , Å	d _{CeO2} , nm	d _{NiO} , nm	d _{Ni} , nm	Δm/m ³ %	Δm/m ⁴ %
Ni/CeMg-C-S-O	12	22	0	8	0	5.402	39	51	No phase	0.04	−0.09
Ni/CeMg-A-S-V	72	87	67	77	1.2	5.399	31	ND ¹	31	−3.0	−0.76
Ni/CeMg-A-S-O	74	75	65	72	1.3	5.402	35	ND ¹	46	0.71	−0.15
Ni-Pd/CeMg-A-S-V	57	64	55	62	1.4	5.399	26	21	16	0.6	−0.36
Ni/CeMg-A-P-O	51	71	49	59	1.1	5.400	47	ND ¹	83	0.69	0.59

¹ Not determined due to low intensity of the peak.

Figure 6 shows data on the stability of catalysts in CSMR depending on the synthesis method and the composition of the active component. A high and stable H_2 yield from 51 to 81% was obtained on the A catalyst, with a one-stage synthesis and activation in a vacuum being preferable to the polyol method and calcination in air. It was established [32] that an important factor providing the catalytic stability of the reduced Ni/MgO was the solid solution without “free” NiO. It can be assumed that preliminary vacuum calcination of the S-samples (one-stage synthesis) ensured the formation of a NiO-MgO solution that was supported by higher values of the crystal lattice parameter (Table 2); therefore, a large amount of Ni^{2+} was in the bulk of the solid solution, which offered strength in the sintering and production of coke. The C-series catalyst exhibited a low activity, which, however, increased over time. According to XRD and XPS data, that sample was not reduced in a 30% H_2/Ar flow at 800 °C (Tables 3 and 4). Apparently, Ni^0 active centers were blocked by salt impurities, which could be removed from the surface by water vapor during the reaction. Thus, the long induction period of the reaction was probably associated with the clearing of active centers and the reduction of Ni^{2+} . At the same time, the quantity of active Ni^0 particles increased with an increase in reaction time from 1 to 6 h, and the H_2 yield increased from 0 to 33%. Pd-promoted catalysts were self-activated under the reaction conditions, as evidenced by an increase in the CH_4 to CO_2 conversion (Figure S8) and in the H_2 yield from 55 to 76% within 2 h of reaction. Such differences between monometallic (Ni/CeO₂) and bimetallic (Pt-Ni/CeO₂) catalysts were also observed in DMR [15]. This was consistent with the coating of the reduced catalyst with chemisorbed hydrogen. The activity of the promoted catalysts was retained during the day of operation, which indicated that they were promising for the CSMR reaction.

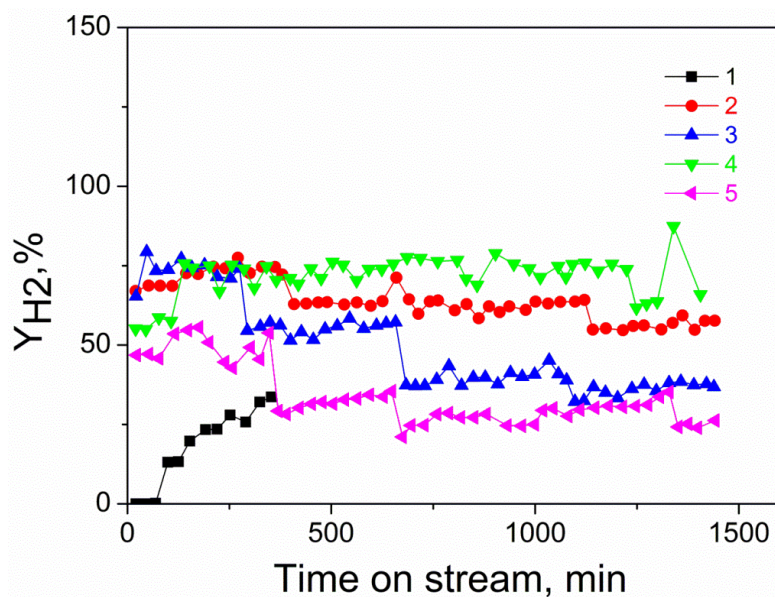


Figure 6. Hydrogen yield during CSMR at 750 °C. 1—Ni/CeMg-C-S-O; 2—Ni/CeMg-A-S-V; 3—Ni/CeMg-A-S-O; 4—Ni-Pd/CeMg-A-S-V; 5—Ni/CeMg-A-P-O.

The activity of catalysts during long-term testing was controlled by two processes: the sintering of nanoparticles and carbon formation. The extent of nickel leaching from the catalyst was negligible due to the strong MSI. The mass of carbon deposited on spent catalysts was calculated from the TGA (Figure 7). A weight loss was observed in the low-temperature range associated with the desorption of volatile reaction compounds, mainly water. In the range from 200 to 325 °C, the weight loss was associated with the removal of the template applied in the synthesis, which was confirmed by the thermal analysis data of fresh catalysts. In addition, in the higher temperature range of 325–470 °C, an increase in the sample weight occurred, accompanied by an exothermic effect ($T_{DTA} = 390$ °C), which was associated with the oxidation of Ni^0 and the formation of oxide particles.

For the C catalyst (chloride support precursor), no weight increase was observed, which indicated a predominantly oxidized state of nickel and corresponded to XPS and XRD data (Tables 3 and 4). For the A catalyst (cerium acetate support precursor) after activation in vacuum, there was also no weight gain step, which was associated with the removal of a larger amount of template. It is known that a weight loss above 470 °C on the TG-DTA curves indicates the formation of coke [64] on the catalysts. The rate of carbon formation in the A catalysts rose in the following order: Ni/CeMg-A-P-O < Ni/CeMg-A-S-O < Ni-Pd/CeMg-A-S-V < Ni/CeMg-A-S-V (Figure 7). Despite the larger amount of deposited carbon, the catalyst activated in vacuum (Table 4) showed a relatively stable CH₄ conversion compared with the catalysts after activation in air. The average crystallite sizes of the spent catalysts were calculated from XRD (Table 3). The XRD pattern of the spent catalysts is displayed in Figure 8. In Ni-Pd/CeMg-A-S-V, a small amount of the Ni⁰ phase was detected by XRD, probably due to the reoxidation of fine particles of metallic nickel upon contact with air, which is consistent with the XPS data.

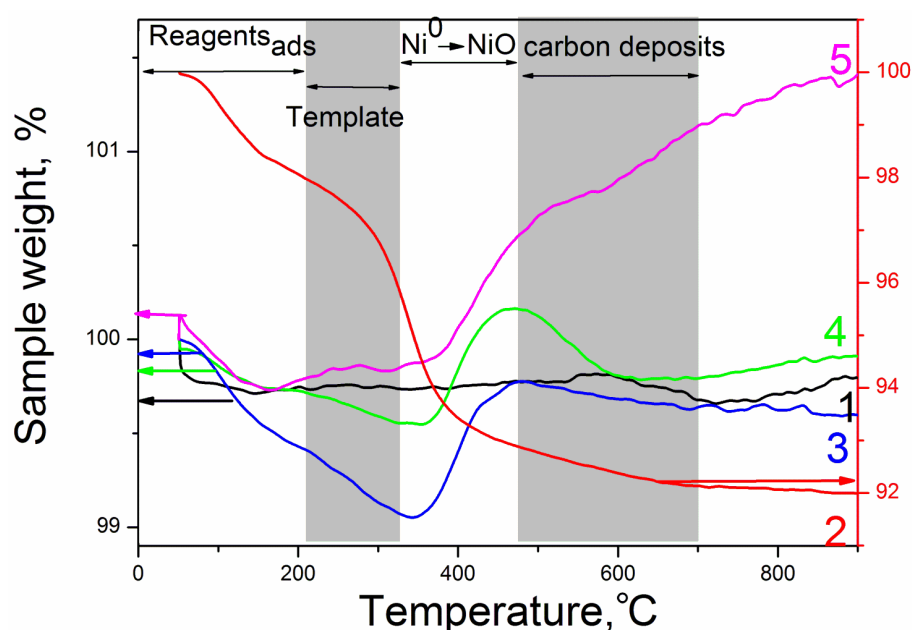


Figure 7. TGA profiles for the catalysts after the CSMR reaction at 750 °C. 1—Ni/CeMg-C-S-O; 2—Ni/CeMg-A-S-V; 3—Ni/CeMg-A-S-O; 4—Ni-Pd/CeMg-A-S-V; 5—Ni/CeMg-A-P-O.

Peaks related to deposited carbon (ICSD 53781) were observed in particular in the Ni-Pd/CeMg-A-S-V and Ni/CeMg-A-S-V catalysts, in agreement with the TGA results. No NaCl phase was observed in spent catalysts, which confirmed the removal of salt during the reaction. The intensity of the Ni⁰ diffraction peak increased compared to reduced catalysts that could result from an increase in the quantity of the metallic Ni and the coarsening of crystallites due to sintering. It is noted that, in contrast to the spent catalysts of the A series, in the spent C catalyst, there was no Ni⁰ phase, which explained its low activity (Figure 5). The Ni crystallite size in the spent A catalysts increased in the next sequence: Ni-Pd/CeMg-A-S-V (16 nm) < Ni/CeMg-A-S-V (31 nm) < Ni/CeMg-A-S-O (46 nm) < Ni/CeMg-A-P-O (83 nm). The Ni-Pd/CeMg-A-S-V and Ni/CeMg-A-S-V samples with a lower rate of deactivation had a higher quantity of carbon deposits. This meant that these differences in the stability of the samples were caused by the differences in their agglomeration properties not in their coking resistance. The weak interaction of Ni with the support and the low thermal stability of the support in the A-S-O catalyst caused a Ni agglomeration upon thermal treatment (Table 3), which also led to its deactivation during the reaction. As a result, at the earlier stage of the reaction, the A-S-O catalyst displayed a high activity, while the A-S-O catalyst was deactivated faster with time on stream than the A-S-V catalysts. It was shown in [65] that the oxygen storage capacity was a secondary

factor influencing the catalytic efficiency. It was established that mobile oxygen inhibited carbon formation by reacting with carbon and improved catalytic performance [23,25,66]. The effectiveness of the carbon removal mechanism depends on CDO and the metal particle size [67]. The CDO effect is strengthened by heavily dispersed metallic particles deposited on reducible oxides and having a higher metal–support interface. In comparison to the Ni/CeMg-A-S-V sample, Ni-Pd/CeMg-A-S-V was characterized by a higher dispersion, CDO, and a lower amount of deposited carbon.

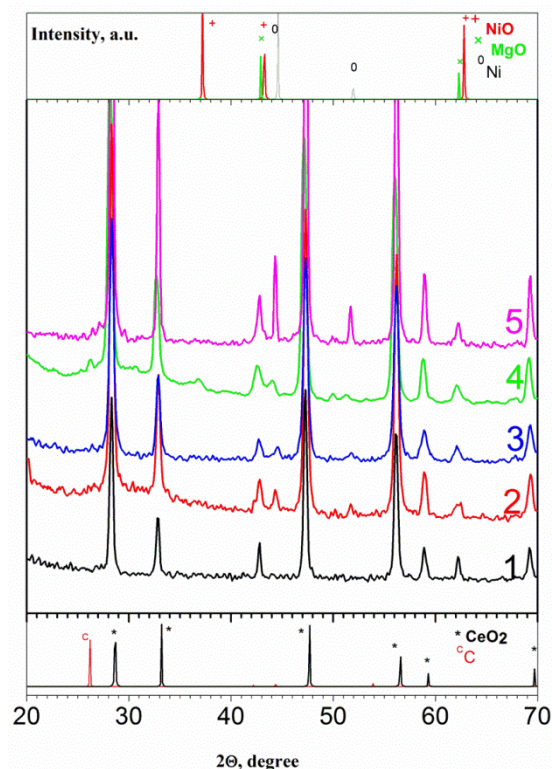


Figure 8. X-ray diffraction patterns of the catalysts after the CSMR reaction at 750 °C. 1—Ni/CeMg-C-S-O; 2—Ni/CeMg-A-S-V; 3—Ni/CeMg-A-S-O; 4—Ni-Pd/CeMg-A-S-V; 5—Ni/CeMg-A-P-O.

The Ni/CeMg-A-P-O (P-series) exhibited the lowest amount of deposited carbon after the reaction. This could be attributed to a lower dispersion and agglomeration of the active component during CSMR and was consistent with the lower thermal stability (Table 3) and MSI. The carbon deposition rate decreased for Ni particles larger than 30 nm and was insignificant for particles with a size of 100 nm [67].

The HRTEM data confirmed the results of the XRD and TA. For spent Ni-Pd/CeMg-A-S-V, the sample contained two types of active component: 15–25 nm in size and clusters consisting of several atoms (Figure 9). HAADF-STEM with an EDX analysis showed (Figure 10) that the CeO₂ and MgO regions were present in the samples. These inhomogeneities were due to the complete destruction of the solid solution. Analogous results have been reported by Matus et al. [28], who prepared a (CeMg)_{1-x}Ni_xO_y catalyst (Ce/MgO = 0.25 – 1) by a polymerized complex method. The combination of the HAADF-STEM images and the STEM-EDX results allowed the identification of the active component phase. Three various kinds of active phase could be clearly identified: low-dispersed particles with a size of 15–25 nm, which corresponded to metallic Ni; then, the second type of bimetallic NiPd nanoparticles with a size of <10 nm (Figure 11); and finally, clusters located in the structure of MgO indicating the formation of a Ni-Mg-O solution (Figure 9) after the calcination step. Pd doping affects metal dispersion at two stages of the catalyst synthesis. Firstly, Pd acted as a nucleus for the reduction and growth of Ni particles in the polyol method. The three phases were identified in the XRD pattern for Ni_{0.97}Pd_{0.03} colloid calcined at 300 °C in vacuum at 10 mbar: an unidentified phase with interplanar spacings of

7.96, 4.07, and 2.61 with an average CSR size of 1.5 nm, the Ni_3C phase (PDF #04-0853) with a particle size of 14 to 17 nm, and a NiPd alloy (ICSD, CC = 670, 625) with an alloy particle size of 4 nm (Figure S9). Secondly, Pd stabilized the surface structure of active ensembles during the reduction treatment and the CSMR process. Note that the monometallic catalyst prepared from the nickel colloid showed an unexpectedly low activity and stability.

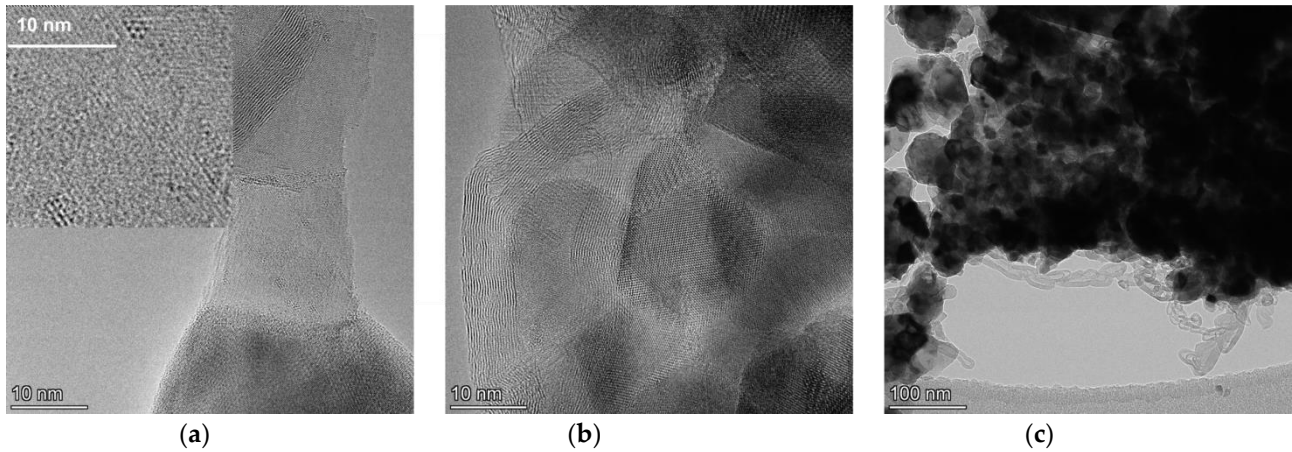


Figure 9. (a,b) HRTEM and (c) TEM images of the spent Ni-Pd/CeMg-A-S-V catalysts.

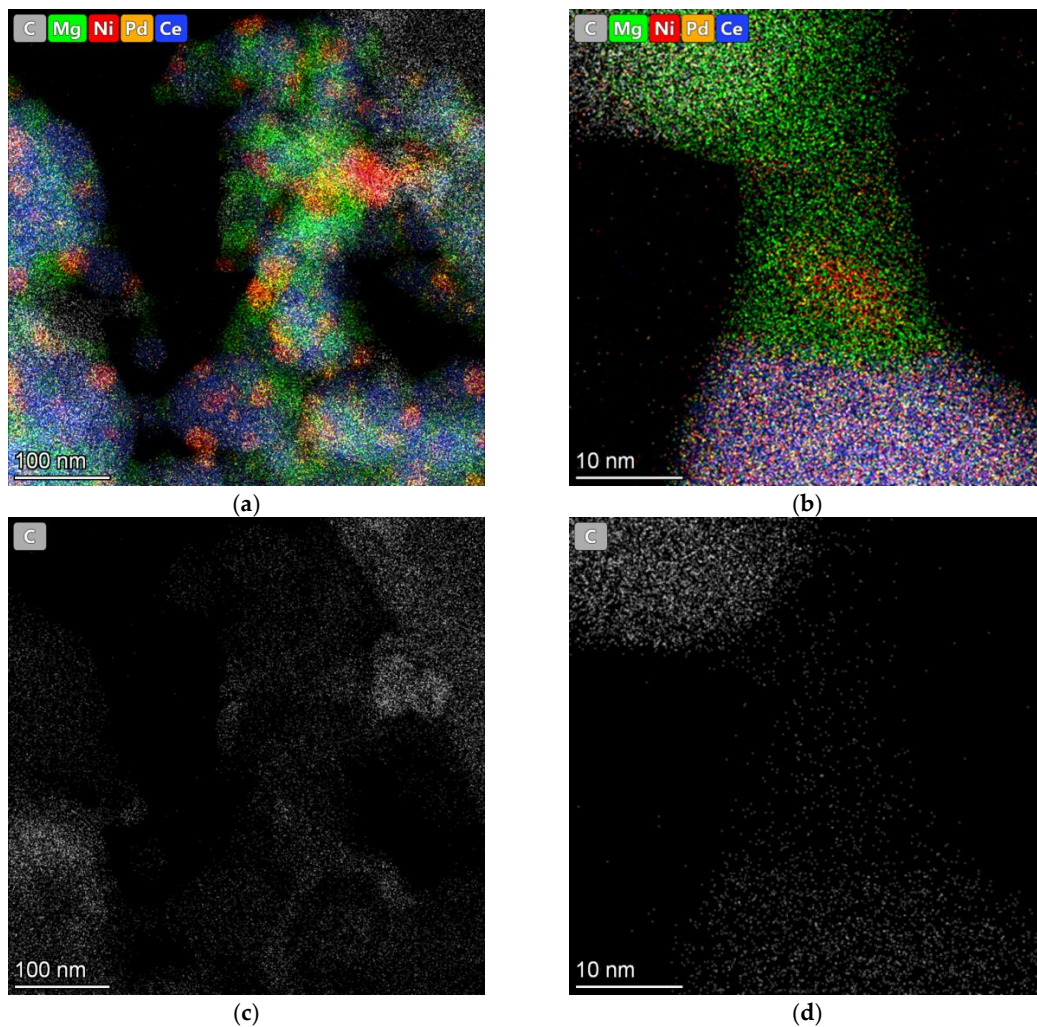


Figure 10. EDX mapping of the (a,b) spent Ni-Pd/CeMg-A-S-V catalysts, (c,d) C elemental map.

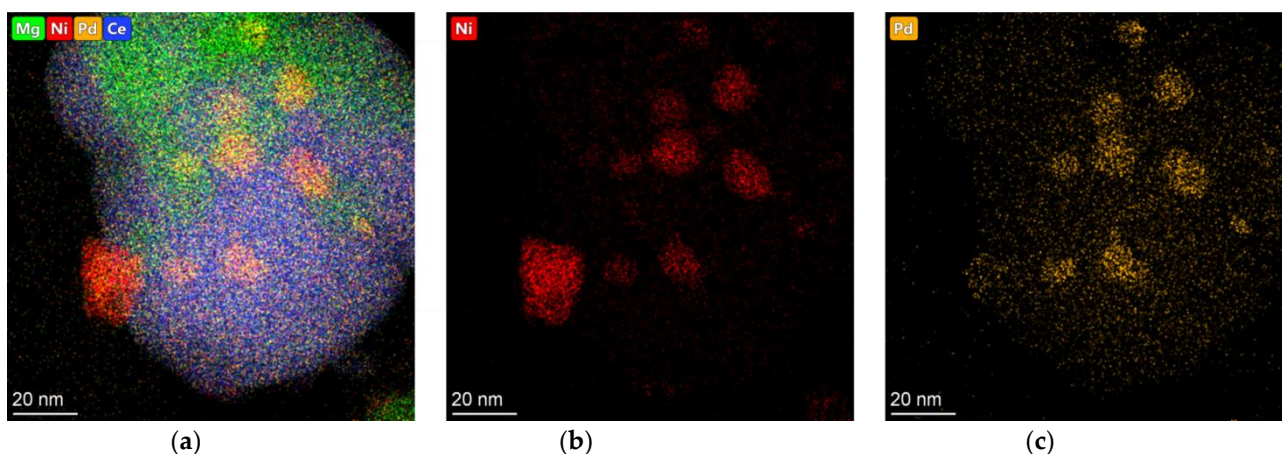


Figure 11. EDX mapping of the (a) spent Ni-Pd/CeMg-A-S-V, (b) Ni elemental map, (c) Pd elemental map.

Carbon deposits were found on the surface of low-dispersed nickel metal particles. No carbon deposits were found on Ni clusters in the MgO site and/or on NiPd nanoparticles (Figure 10). Ni particles formed as a result of such a reductive partial extraction of Ni^{2+} ions in a solid solution will have a fairly strong interaction with the NiO-MgO support and a strength in sintering resistance and coke generation [37,68]. The size of nickel crystallites impacted the quantity and nature of carbon deposition. A higher metal–support interface prevents the carbon formation or promotes the combustion of carbon from the catalyst surface due to an increased oxygen migration from the substrate to the metal surface [67]. Moreover, alloying Ni with noble metals or the very close location of the noble metal to the active Ni species is an effective way to increase catalytic stability due to breaking the C-H bond in such a way that carbon deposition is reduced [69]. From these images, it can be concluded that the highly dispersed NiPd particles and the Ni clusters in MgO provided a high resistance of the catalyst to sintering and the forming of carbon. Even if the particles were covered by carbon, the stability and activity of this catalyst were excellent, indicating that highly dispersed Ni and NiPd particles were responsible for the catalytic performance. It would be expected that catalysts with a lower nickel content would be efficient for the reaction. Note that doping with Mg improved their thermostability at sintering and magnified the Ni–support interaction. On the other hand, the tolerance to carbon deposits was enhanced for CeO_2 -based catalysts without doping, compared to $\text{Ce}_{0.2}\text{Mg}_{0.7}\text{Ni}_{0.1}\text{O}_{1.2}$, which can be associated with a decrease in the oxygen mobility at a higher concentration of dopant [28]. Experiments concerning CeO_2 -MgO with an optimal amount of Mg are in progress to develop more effective catalysts.

The Ni-Pd/CeMg-A-S-V catalyst had a higher dispersion which prevented the formation of carbon, a lower rate of particle sintering, and a higher concentration of defective oxygen. From the point of view of catalytic properties, the Ni-Pd/CeMg-A-S-V catalyst was most effective among the catalysts prepared, as a result of its proper physicochemical properties. This catalyst provided a high yield of target products ($X_{\text{CH}_4} = 73\%$, $X_{\text{CO}_2} = 73\%$, $Y_{\text{H}_2} = 79\%$, and $Y_{\text{CO}} = 71\%$) when tested for stability for 15 h at 750 °C. The achieved process parameters were below the thermodynamic equilibrium values ($X_{\text{CH}_4} = 94\%$, $X_{\text{CO}_2} = 82\%$, $Y_{\text{H}_2} = 83\%$ and $Y_{\text{CO}} = 87\%$) [49] but were comparable with the process parameters described in the literature [32]. Noble metals can promote the reduction and dispersion of the active phase through the overflow effect [37], and facilitate the gasification of surface carbon, providing a high oxygen content on the surface [15]. Such effect was attributed to the formation of a Ce-Pt-O solution promoting the mobility of lattice oxygen and consequently the activity of the carbon oxidation.

4. Conclusions

The use of SGT technology in the preparation of a nickel catalyst based on magnesium-modified cerium oxide $\text{Ce}_{0.5}\text{Mg}_{0.5}\text{O}_{1.5}$ for the combined steam and CO_2 reforming of methane made it possible to obtain nanocrystalline samples characterized by narrow pores (5–10 nm) and an increased thermal stability due to the inhibition of crystallite growth in the support. It was shown by the N_2 adsorption at 77 K and XRD that the dispersion of the active component was controlled by the pore size of the support, the thermal stability of the mesoporous structure of the support, and the method of its functionalization and activation, and increased when cerium acetate was used as a support precursor, with a one-stage synthesis and preliminary activation in vacuum at 300 °C. The efficiency of catalysts in CSMR increased with an increase in the dispersion of the active component, an increase in the concentration of defective oxygen, and when well-dispersed NiPd nanoparticles and clusters of Ni in the MgO phase were formed. The $\text{Ni}_{0.194}\text{Pd}_{0.006}\text{Ce}_{0.4}\text{Mg}_{0.4}\text{O}_{1.4}$ catalyst had the highest dispersion and CDO, ensuring the resistance of the Ni active component to sintering and a stable operation. The yield of the target products was 79% with a conversion of reagents of at least 73% at 750 °C for 15 h of operation.

Supplementary Materials: The following supporting information can be downloaded at: <https://www.mdpi.com/article/10.3390/app13084689/s1>, Physicochemical methods for studying catalysts; Figure S1: Photograph images of the CSMR (a) experimental equipment and (b) reactor, Figure S2: N_2 adsorption–desorption isotherms (a) and pore size distributions (b) of as-prepared catalysts calcined at 500 °C. 1–Ni/CeMg-C-S-O; 2–Ni/CeMg-A-S-V; 3–Ni/CeMg-A-S-O; 4–Ni-Pd/CeMg-A-S-V; 5–Ni/CeMg-A-P-O, Figure S3: SEM images Ni/CeMg-C-S-O, Figure S4: X-ray diffraction patterns of the as-prepared catalysts calcined at 500 °C. 1–Ni/CeMg-C-S-O; 2–Ni/CeMg-A-S-V; 3–Ni/CeMg-A-S-O; 4–Ni-Pd/CeMg-A-S-V; 5–Ni/CeMg-A-P-O, Figure S5: Survey X-ray photoelectron spectra of reduced catalysts. 1–Ni/CeMg-C-S-O; 2–Ni/CeMg-A-S-V; 3–Ni/CeMg-A-S-O; 4–Ni-Pd/CeMg-A-S-V; 5–Ni/CeMg-A-P-O, Figure S6: X-ray photoelectron spectra of Ni2p over reduced catalysts. 1–Ni/CeMg-C-S-O; 2–Ni/CeMg-A-S-V; 3–Ni/CeMg-A-S-O; 4–Ni-Pd/CeMg-A-S-V; 5–Ni/CeMg-A-P-O, Figure S7: Temperature dependence of CO_2 and CH_4 conversions and H_2 and CO yields on catalyst Ni/CeMg-C-S-O, Figure S8: CH_4 conversion (a), CO_2 conversion (b), CO yield (c), and H_2/CO ratio (d) during CSMR at 750 °C over M/ $\text{Ce}_{0.5}\text{Mg}_{0.5}\text{O}_{1.5}$. 1–Ni/CeMg-C-S-O; 2–Ni/CeMg-A-S-V; 3–Ni/CeMg-A-S-O; 4–Ni-Pd/CeMg-A-S-V; 5–Ni/CeMg-A-P-O, Figure S9. Diffraction patterns of colloids stabilized by PVP and calcined at 573 K in vacuum at 10 mbar: Ni_{0.97}Pd_{0.03} (1), Ni (2), Pd (3).

Author Contributions: Conceptualization, L.O.; methodology, L.O.; software, I.P.; validation, L.O.; formal analysis, L.O.; investigation, I.P.; resources L.O.; data curation, L.O.; writing—original draft preparation, L.O.; writing—review and editing, M.K.; visualization, I.P.; supervision, Z.I.; project administration, Z.I.; funding acquisition, M.K. All authors have read and agreed to the published version of the manuscript.

Funding: This research was funded by the Ministry of Science and Higher Education of the Russian Federation within the governmental order for the Boreskov Institute of Catalysis (grant number project AAAA-A21-121011490008-3).

Institutional Review Board Statement: Not applicable.

Informed Consent Statement: Not applicable.

Data Availability Statement: Data is contained within the article.

Acknowledgments: The authors are grateful to Ushakov V.A., Efimenko T.Ya., Kraevskaya I.L. and Ishenko A.V. for their assistance in the study of samples by physicochemical methods and Sukhova O.B. for the catalytic experiments.

Conflicts of Interest: The authors declare no conflict of interest.

References

1. Hosseini, S.E.; Wahid, M.A. Hydrogen Production from Renewable and Sustainable Energy Resources: Promising Green Energy Carrier for Clean Development. *Renew. Sustain. Energy Rev.* **2016**, *57*, 850–866. [[CrossRef](#)]
2. Nikolaidis, P.; Poullikkas, A. A Comparative Overview of Hydrogen Production Processes. *Renew. Sustain. Energy Rev.* **2017**, *67*, 597–611. [[CrossRef](#)]
3. Usman, M.; Wan Daud, W.M.A.; Abbas, H.F. Dry Reforming of Methane: Influence of Process Parameters—A Review. *Renew. Sustain. Energy Rev.* **2015**, *45*, 710–744. [[CrossRef](#)]
4. Da Fonseca, R.O.; Rabelo-Neto, R.C.; Simões, R.C.C.; Mattos, L.V.; Noronha, F.B. Pt Supported on Doped CeO₂/Al₂O₃ as Catalyst for Dry Reforming of Methane. *Int. J. Hydrog. Energy* **2020**, *45*, 5182–5191. [[CrossRef](#)]
5. Lu, Y.; Lee, T. Influence of the Feed Gas Composition on the Fischer-Tropsch Synthesis in Commercial Operations. *J. Nat. Gas Chem.* **2007**, *16*, 329–341. [[CrossRef](#)]
6. Peng, X.; Cheng, K.; Kang, J.; Gu, B.; Yu, X.; Zhang, Q.; Wang, Y. Impact of Hydrogenolysis on the Selectivity of the Fischer-Tropsch Synthesis: Diesel Fuel Production over Mesoporous Zeolite-Y-Supported Cobalt Nanoparticles. *Angew. Chemie—Int. Ed.* **2015**, *54*, 4553–4556. [[CrossRef](#)]
7. Xia, Y.; Lu, N.; Li, J.; Jiang, N.; Shang, K.; Wu, Y. Combined Steam and CO₂ Reforming of CH₄ for Syngas Production in a Gliding Arc Discharge Plasma. *J. CO₂ Util.* **2020**, *37*, 248–259. [[CrossRef](#)]
8. Batebi, D.; Abedini, R.; Mosayebi, A. Combined Steam and CO₂ Reforming of Methane (CSCRM) over Ni-Pd/Al₂O₃ Catalyst for Syngas Formation. *Int. J. Hydrog. Energy* **2020**, *45*, 14293–14310. [[CrossRef](#)]
9. De Araújo Moreira, T.G.; de Carvalho Filho, J.F.S.; Carvalho, Y.; de Almeida, J.M.A.R.; Nothaft Romano, P.; Falabella Sousa-Aguiar, E. Highly Stable Low Noble Metal Content Rhodium-Based Catalyst for the Dry Reforming of Methane. *Fuel* **2021**, *287*, 119536. [[CrossRef](#)]
10. De Caprariis, B.; De Filippis, P.; Palma, V.; Petrullo, A.; Ricca, A.; Ruocco, C.; Scarsella, M. Rh, Ru and Pt Ternary Perovskites Type Oxides BaZr(1-x)MexO₃ for Methane Dry Reforming. *Appl. Catal. A Gen.* **2016**, *517*, 47–55. [[CrossRef](#)]
11. Mahfouz, R.; Estephane, J.; Gennequin, C.; Tidahy, L.; Aouad, S.; Abi-Aad, E. CO₂ reforming of Methane over Ni and/or Ru Catalysts Supported on Mesoporous KIT-6: Effect of Promotion with Ce. *J. Environ. Chem. Eng.* **2021**, *9*, 104662. [[CrossRef](#)]
12. Singha, R.K.; Yadav, A.; Shukla, A.; Kumar, M.; Bal, R. Low Temperature Dry Reforming of Methane over Pd-CeO₂ Nanocatalyst. *Catal. Commun.* **2017**, *92*, 19–22. [[CrossRef](#)]
13. Yue, L.; Li, J.; Chen, C.; Fu, X.; Gong, Y.; Xia, X.; Hou, J.; Xiao, C.; Chen, X.; Zhao, L.; et al. Thermal-Stable Pd@mesoporous Silica Core-Shell Nanocatalysts for Dry Reforming of Methane with Good Coke-Resistant Performance. *Fuel* **2018**, *218*, 335–341. [[CrossRef](#)]
14. Anil, C.; Modak, J.M.; Madras, G. Syngas Production via CO₂ Reforming of Methane over Noble Metal (Ru, Pt, and Pd) Doped LaAlO₃ Perovskite Catalyst. *Mol. Catal.* **2020**, *484*, 110805. [[CrossRef](#)]
15. Araiza, D.G.; Arcos, D.G.; Gómez-Cortés, A.; Díaz, G. Dry Reforming of Methane over Pt-Ni/CeO₂ Catalysts: Effect of the Metal Composition on the Stability. *Catal. Today* **2021**, *360*, 46–54. [[CrossRef](#)]
16. Bahari, M.B.; Setiabudi, H.D.; Ainirazali, N.; Vo, D.-V.N. A Short Review on Bimetallic Co-Based Catalysts for Carbon Dioxide Reforming of Methane. *Mater. Today Proc.* **2021**, *42*, 94–100. [[CrossRef](#)]
17. Abasaeed, A.E.; Al-Fatesh, A.S.; Naem, M.A.; Ibrahim, A.A.; Fakeeha, A.H. Catalytic Performance of CeO₂ and ZrO₂ Supported Co Catalysts for Hydrogen Production via Dry Reforming of Methane. *Int. J. Hydrog. Energy* **2015**, *40*, 6818–6826. [[CrossRef](#)]
18. Sengupta, S.; Deo, G. Modifying Alumina with CaO or MgO in Supported Ni and Ni-Co Catalysts and Its Effect on Dry Reforming of CH₄. *J. CO₂ Util.* **2015**, *10*, 67–77. [[CrossRef](#)]
19. Zhang, T.; Liu, Z.; Zhu, Y.A.; Liu, Z.; Sui, Z.; Zhu, K.; Zhou, X. Dry Reforming of Methane on Ni-Fe-MgO Catalysts: Influence of Fe on Carbon-Resistant Property and Kinetics. *Appl. Catal. B Environ.* **2020**, *264*, 118497. [[CrossRef](#)]
20. Kim, H.M.; Jang, W.J.; Yoo, S.Y.; Shim, J.O.; Jeon, K.W.; Na, H.S.; Lee, Y.L.; Jeon, B.H.; Bae, J.W.; Roh, H.S. Low Temperature Steam Reforming of Methane Using Metal Oxide Promoted Ni-Ce_{0.8}Zr_{0.2}O₂ Catalysts in a Compact Reformer. *Int. J. Hydrog. Energy* **2018**, *43*, 262–270. [[CrossRef](#)]
21. Solymosi, F.; Kutsán, G.; Erdöhelyi, A. Catalytic Reaction of CH₄ with CO₂ over Alumina-Supported Pt Metals. *Catal. Letters* **1991**, *11*, 149–156. [[CrossRef](#)]
22. Khajenoori, M.; Rezaei, M.; Meshkani, F. Characterization of CeO₂ Promoter of a Nanocrystalline Ni/MgO Catalyst in Dry Reforming of Methane. *Chem. Eng. Technol.* **2014**, *37*, 957–963. [[CrossRef](#)]
23. Cao, L.; Ni, C.; Yuan, Z.; Wang, S. Correlation between Catalytic Selectivity and Oxygen Storage Capacity in Autothermal Reforming of Methane over Rh/Ce_{0.45}Zr_{0.45}RE_{0.1} Catalysts (RE = La, Pr, Nd, Sm, Eu, Gd, Tb). *Catal. Commun.* **2009**, *10*, 1192–1195. [[CrossRef](#)]
24. Hussain, I.; Tanimu, G.; Ahmed, S.; Aniz, C.U.; Alasiri, H.; Alhooshani, K. A Review of the Indispensable Role of Oxygen Vacancies for Enhanced CO₂ Methanation Activity over CeO₂-Based Catalysts: Uncovering, Influencing, and Tuning Strategies. *Int. J. Hydrogen Energy* **2022**, *in press*. [[CrossRef](#)]
25. Li, P.; Chen, X.; Li, Y.; Schwank, J.W. A Review on Oxygen Storage Capacity of CeO₂-Based Materials: Influence Factors, Measurement Techniques, and Applications in Reactions Related to Catalytic Automotive Emissions Control. *Catal. Today* **2019**, *327*, 90–115. [[CrossRef](#)]

26. Zhang, Q.H.; Li, Y.; Xu, B.Q. Reforming of Methane and Coalbed Methane over Nanocomposite Ni/ZrO₂ Catalyst. *Catal. Today* **2004**, *98*, 601–605. [[CrossRef](#)]
27. Roh, H.S.; Koo, K.Y.; Jeong, J.H.; Seo, Y.T.; Seo, D.J.; Seo, Y.S.; Yoon, W.L.; Park, S. Bin Combined Reforming of Methane over Supported Ni Catalysts. *Catal. Letters* **2007**, *117*, 85–90. [[CrossRef](#)]
28. Matus, E.; Sukhova, O.; Kerzhentsev, M.; Ismagilov, I.; Yashnik, S.; Ushakov, V.; Stonkus, O.; Gerasimov, E.; Nikitin, A.; Bharali, P.; et al. Hydrogen Production through Bi-Reforming of Methane: Improving Ni Catalyst Performance via an Exsolution Approach. *Catalysts* **2022**, *12*, 1493. [[CrossRef](#)]
29. Lucrédio, A.F.; Assaf, J.M.; Assaf, E.M. Methane Conversion Reactions on Ni Catalysts Promoted with Rh: Influence of Support. *Appl. Catal. A Gen.* **2011**, *400*, 156–165. [[CrossRef](#)]
30. Özdemir, H.; Faruk Öksüzömer, M.A.; Ali Gürkaynak, M. Preparation and Characterization of Ni Based Catalysts for the Catalytic Partial Oxidation of Methane: Effect of Support Basicity on H₂/CO Ratio and Carbon Deposition. *Int. J. Hydrog. Energy* **2010**, *35*, 12147–12160. [[CrossRef](#)]
31. Jeon, K.W.; Kim, H.M.; Kim, B.J.; Lee, Y.L.; Na, H.S.; Shim, J.O.; Jang, W.J.; Roh, H.S. Synthesis Gas Production from Carbon Dioxide Reforming of Methane over Ni-MgO Catalyst: Combined Effects of Titration Rate during Co-Precipitation and CeO₂ Addition. *Fuel Process. Technol.* **2021**, *219*, 106877. [[CrossRef](#)]
32. Wang, Y.H.; Liu, H.M.; Xu, B.Q. Durable Ni/MgO Catalysts for CO₂ Reforming of Methane: Activity and Metal-Support Interaction. *J. Mol. Catal. A Chem.* **2009**, *299*, 44–52. [[CrossRef](#)]
33. Bukhari, S.N.; Chin, C.Y.; Setiabudi, H.D.; Vo, D.V.N. Tailoring the Properties and Catalytic Activities of Ni/SBA-15 via Different TEOS/P123 Mass Ratios for CO₂ Reforming of CH₄. *J. Environ. Chem. Eng.* **2017**, *5*, 3122–3128. [[CrossRef](#)]
34. Zhang, Q.; Zhang, T.; Shi, Y.; Zhao, B.; Wang, M.; Liu, Q.; Wang, J.; Long, K.; Duan, Y.; Ning, P. A Sintering and Carbon-Resistant Ni-SBA-15 Catalyst Prepared by Solid-State Grinding Method for Dry Reforming of Methane. *J. CO₂ Util.* **2017**, *17*, 10–19. [[CrossRef](#)]
35. Muraleedharan Nair, M.; Kaliaguine, S. Structured Catalysts for Dry Reforming of Methane. *New J. Chem.* **2016**, *40*, 4049–4060. [[CrossRef](#)]
36. Li, D.; Nakagawa, Y.; Tomishige, K. Methane Reforming to Synthesis Gas over Ni Catalysts Modified with Noble Metals. *Appl. Catal. A Gen.* **2011**, *408*, 1–24. [[CrossRef](#)]
37. Pan, C.; Guo, Z.; Dai, H.; Ren, R.; Chu, W. Anti-Sintering Mesoporous Ni-Pd Bimetallic Catalysts for Hydrogen Production via Dry Reforming of Methane. *Int. J. Hydrog. Energy* **2020**, *45*, 16133–16143. [[CrossRef](#)]
38. Nurunnabi, M.; Fujimoto, K.I.; Suzuki, K.; Li, B.; Kado, S.; Kunitomi, K.; Tomishige, K. Promoting Effect of Noble Metals Addition on Activity and Resistance to Carbon Deposition in Oxidative Steam Reforming of Methane over NiO-MgO Solid Solution. *Catal. Commun.* **2006**, *7*, 73–78. [[CrossRef](#)]
39. Jeong, J.H.; Lee, J.W.; Seo, D.J.; Seo, Y.; Yoon, W.L.; Lee, D.K.; Kim, D.H. Ru-Doped Ni Catalysts Effective for the Steam Reforming of Methane without the Pre-Reduction Treatment with H₂. *Appl. Catal. A Gen.* **2006**, *302*, 151–156. [[CrossRef](#)]
40. Trovarelli, A. Catalytic Properties of Ceria and CeO₂-Containing Materials. *Catal. Rev.—Sci. Eng.* **1996**, *38*, 439–520. [[CrossRef](#)]
41. Yoon, Y.; Kim, H.; Lee, J. Enhanced Catalytic Behavior of Ni Alloys in Steam Methane Reforming. *J. Power Sources* **2017**, *359*, 450–457. [[CrossRef](#)]
42. Xi, J.; Wang, Q.; Duan, X.; Zhang, N.; Yu, J.; Sun, H.; Wang, S. Continuous Flow Reduction of Organic Dyes over Pd-Fe Alloy Based Fibrous Catalyst in a Fixed-Bed System. *Chem. Eng. Sci.* **2021**, *231*, 116303. [[CrossRef](#)]
43. Zhang, Y.; Huang, J.; Dong, Z.; Zhan, Y.; Xi, J.; Xiao, J.; Huang, S.; Tian, F. Pd-Fe Bimetallic Nanoparticles Anchored on N-Doped Carbon-Modified Graphene for Efficient Catalytic Organic Reactions. *Carbon Lett.* **2022**, *33*, 77–87. [[CrossRef](#)]
44. Wang, D.; Li, Y.; Wen, L.; Xi, J.; Liu, P.; Hansen, T.W.; Li, P. Ni-Pd-Incorporated Fe₃O₄ Yolk-Shelled Nanospheres as Efficient Magnetically Recyclable Catalysts for Reduction of N-Containing Unsaturated Compounds. *Catalysts* **2023**, *13*, 190. [[CrossRef](#)]
45. Zhang, N.; Qiu, Y.; Sun, H.; Hao, J.; Chen, J.; Xi, J.; Liu, J.; He, B.; Bai, Z.-W. Substrate-Assisted Encapsulation of Pd-Fe Bimetal Nanoparticles on Functionalized Silica Nanotubes for Catalytic Hydrogenation of Nitroarenes and Azo Dyes. *ACS Appl. Nano Mater.* **2021**, *4*, 5854–5863. [[CrossRef](#)]
46. Wen, L.; Wang, D.; Xi, J.; Tian, F.; Liu, P.; Bai, Z.W. Heterometal Modified Fe₃O₄ Hollow Nanospheres as Efficient Catalysts for Organic Transformations. *J. Catal.* **2022**, *413*, 779–785. [[CrossRef](#)]
47. Matus, V.; Sukhova, O.B.; Ismagilov, I.Z.; Ushakov, V.A.; Yashnik, S.A.; Kerzhentsev, M.A.; Ismagilov, Z.R. Steam/CO₂ Reforming of Methane Over Impregnated Ni/CeO₂ Catalysts: Effect of Sample Composition on Their Activity and Stability. *Eurasian Chem. J.* **2022**, *24*, 191–202. [[CrossRef](#)]
48. Okhlopko, L.B.; Kerzhentsev, M.A.; Tuzikov, F.V.; Larichev, Y.V.; Prosvirin, I.P.; Ismagilov, Z.R. Palladium-Zinc Catalysts on Mesoporous Titania Prepared by Colloid Synthesis. I. Size Control Synthesis of PdZn Nanoclusters by a Polyol Method. *J. Nanoparticle Res.* **2012**, *14*, 1089. [[CrossRef](#)]
49. Matus, E.V.; Sukhova, O.B.; Ismagilov, I.Z.; Kerzhentsev, M.A.; Li, L.; Ismagilov, Z.R. Bi-Reforming of Methane: Thermodynamic Equilibrium Analysis and Selection of Preferable Reaction Conditions. *J. Phys. Conf. Ser.* **2021**, *1749*, 012023. [[CrossRef](#)]
50. Nguyen-Phan, T.D.; Song, M.B.; Kim, E.J.; Shin, E.W. The Role of Rare Earth Metals in Lanthanide-Incorporated Mesoporous Titania. *Microporous Mesoporous Mater.* **2009**, *119*, 290–298. [[CrossRef](#)]

51. Yao, S.Y.; Xu, W.Q.; Johnston-Peck, A.C.; Zhao, F.Z.; Liu, Z.Y.; Luo, S.; Senanayake, S.D.; Martínez-Arias, A.; Liu, W.J.; Rodriguez, J.A. Morphological Effects of the Nanostructured Ceria Support on the Activity and Stability of CuO/CeO₂ Catalysts for the Water-Gas Shift Reaction. *Phys. Chem. Chem. Phys.* **2014**, *16*, 17183–17195. [[CrossRef](#)] [[PubMed](#)]
52. Khalesi, A.; Arandiyani, H.R.; Parvari, M. Production of Syngas by CO₂ Reforming on M_xLa_{1-x}Ni_{0.3}Al_{0.7}O_{3-d} (M = Li, Na, K) Catalysts. *Ind. Eng. Chem. Res.* **2008**, *47*, 5892–5898. [[CrossRef](#)]
53. Matus, E.V.; Okhlopkova, L.B.; Sukhova, O.B.; Ismagilov, I.Z.; Kerzhentsev, M.A.; Ismagilov, Z.R. Effects of Preparation Mode and Doping on the Genesis and Properties of Ni/Ce_{1-x}M_xO_y Nanocrystallites (M = Gd, La, Mg) for Catalytic Applications. *J. Nanoparticle Res.* **2019**, *21*, 11. [[CrossRef](#)]
54. Zhiming, G.A.O.; Shan, Z.; Hongwei, M.A.; Zhanping, L.I. Surface Composition Change of Chlorine-Doped Catalyst Ni (Cl_x)/CeO₂ in Methanation Reaction. *J. Rare Earths* **2017**, *35*, 977–983. [[CrossRef](#)]
55. Huang, Y.; Long, B.; Tang, M.; Rui, Z.; Balogun, M.S.; Tong, Y.; Ji, H. Bifunctional Catalytic Material: An Ultrastable and High-Performance Surface Defect CeO₂ Nanosheets for Formaldehyde Thermal Oxidation and Photocatalytic Oxidation. *Appl. Catal. B Environ.* **2016**, *181*, 779–787. [[CrossRef](#)]
56. Huang, T.J.; Lin, H.J.; Yu, T.C. A Comparison of Oxygen-Vacancy Effect on Activity Behaviors of Carbon Dioxide and Steam Reforming of Methane over Supported Nickel Catalysts. *Catal. Letters* **2005**, *105*, 239–247. [[CrossRef](#)]
57. Wang, Z.; Yang, L.; Zhang, R.; Li, L.; Cheng, Z.; Zhou, Z. Selective Hydrogenation of Phenylacetylene over Bimetallic Pd-Cu/Al₂O₃ and Pd-Zn/Al₂O₃ Catalysts. *Catal. Today* **2016**, *264*, 37–43. [[CrossRef](#)]
58. Löfberg, A.; Guerrero-Caballero, J.; Kane, T.; Rubbens, A.; Jalowiecki-Duhamel, L. Ni/CeO₂ Based Catalysts as Oxygen Vectors for the Chemical Looping Dry Reforming of Methane for Syngas Production. *Appl. Catal. B Environ.* **2017**, *212*, 159–174. [[CrossRef](#)]
59. Özkara-Aydınoğlu, Ş. Thermodynamic Equilibrium Analysis of Combined Carbon Dioxide Reforming with Steam Reforming of Methane to Synthesis Gas. *Int. J. Hydrog. Energy* **2010**, *35*, 12821–12828. [[CrossRef](#)]
60. Maestri, M.; Vlachos, D.G.; Beretta, A.; Groppi, G.; Tronconi, E. Steam and Dry Reforming of Methane on Rh: Microkinetic Analysis and Hierarchy of Kinetic Models. *J. Catal.* **2008**, *259*, 211–222. [[CrossRef](#)]
61. Shinde, V.M.; Madras, G. Catalytic Performance of Highly Dispersed Ni/TiO₂ for Dry and Steam Reforming of Methane. *RSC Adv.* **2014**, *4*, 4817–4826. [[CrossRef](#)]
62. Wei, J.; Iglesia, E. Structural Requirements and Reaction Pathways in Methane Activation and Chemical Conversion Catalyzed by Rhodium. *J. Catal.* **2004**, *225*, 116–127. [[CrossRef](#)]
63. Jones, G.; Jakobsen, J.G.; Shim, S.S.; Kleis, J.; Andersson, M.P.; Rossmeis, J.; Abild-Pedersen, F.; Bligaard, T.; Helveg, S.; Hinnemann, B.; et al. First Principles Calculations and Experimental Insight into Methane Steam Reforming over Transition Metal Catalysts. *J. Catal.* **2008**, *259*, 147–160. [[CrossRef](#)]
64. Jang, W.J.; Jeong, D.W.; Shim, J.O.; Kim, H.M.; Roh, H.S.; Son, I.H.; Lee, S.J. Combined Steam and Carbon Dioxide Reforming of Methane and Side Reactions: Thermodynamic Equilibrium Analysis and Experimental Application. *Appl. Energy* **2016**, *173*, 80–91. [[CrossRef](#)]
65. Jang, W.J.; Kim, H.M.; Shim, J.O.; Yoo, S.Y.; Jeon, K.W.; Na, H.S.; Lee, Y.L.; Jeong, D.W.; Bae, J.W.; Nah, I.W.; et al. Key Properties of Ni-MgO-CeO₂, Ni-MgO-ZrO₂, and Ni-MgO-Ce_(1-x)Zr_(x)O₂ Catalysts for the Reforming of Methane with Carbon Dioxide. *Green Chem.* **2018**, *20*, 1621–1633. [[CrossRef](#)]
66. Xiang, X.; Zhao, H.; Yang, J.; Zhao, J.; Yan, L.; Song, H.; Chou, L. Nickel Based Mesoporous Silica-Ceria-Zirconia Composite for Carbon Dioxide Reforming of Methane. *Appl. Catal. A Gen.* **2016**, *520*, 140–150. [[CrossRef](#)]
67. Da Fonseca, R.O.; Pongeggi, A.R.; Rabelo-Neto, R.C.; Simões, R.C.C.; Mattos, L.V.; Noronha, F.B. Controlling Carbon Formation over Ni/CeO₂ Catalyst for Dry Reforming of CH₄ by Tuning Ni Crystallite Size and Oxygen Vacancies of the Support. *J. CO₂ Util.* **2022**, *57*, 101880. [[CrossRef](#)]
68. Ruckenstein, E. Binary MgO-Based Solid Solution Catalysts for Methane Conversion to Syngas. *Catal. Rev.—Sci. Eng.* **2002**, *44*, 423–453. [[CrossRef](#)]
69. Singha, R.K.; Shukla, A.; Sandupatla, A.; Deo, G.; Bal, R. Synthesis and Catalytic Activity of a Pd Doped Ni-MgO Catalyst for Dry Reforming of Methane. *J. Mater. Chem. A* **2017**, *5*, 15688–15699. [[CrossRef](#)]

Disclaimer/Publisher's Note: The statements, opinions and data contained in all publications are solely those of the individual author(s) and contributor(s) and not of MDPI and/or the editor(s). MDPI and/or the editor(s) disclaim responsibility for any injury to people or property resulting from any ideas, methods, instructions or products referred to in the content.